



Defect-Enhanced Charge Separation and Transfer within Protection Layer/Semiconductor Structure of Photoanodes

Jianyun Zheng, Yanhong Lyu, Chao Xie, Ruilun Wang, Li Tao, Haibo Wu, Huaijuan Zhou,* Sanping Jiang, and Shuangyin Wang*

Silicon (Si) requires a protection layer to maintain stable and long-time photoanodic reaction. However, poor charge separation and transfer are key constraint factors in protection layer/Si photoanodes that reduce their water-splitting efficiency. Here, a simultaneous enhancement of charge separation and transfer in Nb-doped NiO_x/Ni/black-Si photoanodes induced by plasma treatment is reported. The optimized photoanodes yield the highest charge-separation efficiency (η_{sep}) of $\approx 81\%$ at 1.23 V versus reversible hydrogen electrode, corresponding to the photocurrent density of $\approx 29.1 \text{ mA cm}^{-2}$. On the basis of detailed characterizations, the concentration and species of oxygen defects in the NiO_x-based layer are adjusted by synergistic effect of Nb doping and plasma treatment, which are the dominating factors for forming suitable band structure and providing a favorable hole-migration channel. This work elucidates the important role of oxygen defects on charge separation and transfer in the protection layer/Si-based photoelectrochemical systems and is encouraging for application of this synergistic strategy to other candidate photoanodes.

Traditional high-quality semiconductors (like Si) are excellent light absorbers with high carrier mobilities. Compared with planar Si wafers, Si with a porous surface (also known as black Si) can concurrently minimize light reflection by trapping light inside the surface channels^[4] and increase active area for interfacial reactions.^[5] Nevertheless, enlarged surface area and inherent material instabilities of black Si can accelerate surface corrosion/passivation in aqueous electrolyte. To address this shortcoming, protection layers for segregating unstable black Si from solution have been developed.^[6,7] Ideally, protection layers should facilitate charge separation and transport without impeding photoanode stability. However, the addition of new layers can introduce electrical series resistance and interfacial recombination processes, which further affect charge separation and transfer in black Si-based photoanodes.

Solar-to-chemical energy conversion is one of the primary goals for scientists in the field of solar energy generation.^[1] Photoelectrochemical (PEC) water splitting is such an intriguing way. Tremendous efforts have been invested in the pursuit of photoactive and durable semiconductor materials, especially for photoanodes operating under highly oxidizing potentials.^[2,3]

Ni-oxide films (NiO_x) fabricated by magnetron sputtering have been widely used as protection layers on the photoanode surfaces.^[8–10] The NiO_x layer absorbs hardly visible light from solar irradiation due to a wide bandgap ($>3.0 \text{ eV}$). In addition, NiO_x has an index of refraction that makes it a near-optimal antireflective coating on the semiconductor surface. Furthermore, NiO_x is quite stable in base and is also good electrocatalyst for oxygen evolution reaction (OER), in particular doped with Fe.^[11] NiO_x/Si-based PEC system in previous work has produced high photocurrent densities (J) for OER from water for months of continuous operation under simulated 1 Sun conditions and high applied voltage.^[12] However, owing to nonoptimal energetic at the interface between NiO_x layer and Si-based photoanodes and high bulk resistance (e.g., $1.4 \times 10^{-4} \Omega \text{ cm}$ for NiO),^[7] J at 1.23 V versus reversible hydrogen electrode (RHE) is still relatively low. Significantly higher J values at 1.23 V versus RHE need to be pursued by improving charge separation and transfer. Usually, engineering the interfacial electronic band structure is the most fundamental strategy to tune the charge-separation property of a PEC device. Much research has focused on selective doping or introducing of defects into the lattice of NiO_x to optimize the interfacial band alignment between NiO_x layer and Si-based photoanode.^[13] On the other hand, the presence of conductive defect states in thick protection layers ($>10 \text{ nm}$) can minimize charge extraction barriers and series resistance through the oxide layers to ensure the

Dr. J. Zheng, Dr. Y. Lyu, C. Xie, R. Wang, L. Tao, Prof. S. Wang
State Key Laboratory of Chem/Bio-Sensing and Chemometrics
College of Chemistry and Chemical Engineering
Hunan University
Changsha 410082, Hunan, China
E-mail: shuangyinwang@hnu.edu.cn

Dr. H. Wu, Dr. H. Zhou
State Key Laboratory of High Performance Ceramics
and Superfine Microstructure
Shanghai Institute of Ceramics
Chinese Academy of Sciences
Shanghai 200050, China
E-mail: huaijuanzhou518@mail.sic.ac.cn, zhouhuaijuan518@gmail.com

Prof. S. Jiang
Fuels and Energy Technology Institute and Department
of Chemical Engineering
Curtin University
Perth, Western Australia 6102, Australia

The ORCID identification number(s) for the author(s) of this article can be found under <https://doi.org/10.1002/adma.201801773>.

DOI: 10.1002/adma.201801773

charge-transfer efficiency.^[14] Thus, the simultaneous improvement of charge separation and transfer in NiO_x/Si-based photoanodes can be achieved by integrating the approaches mentioned above. Meanwhile, understanding the enhancement of charge separation and transfer is necessary for designing an efficient protection layer/Si-based photoanode.

We hypothesize that i) a small amount of Nb elements in NbO_x lattice can transfer into NiO_x lattice to replace Ni sites under external force because of similar atomic radius, and ii) by controlling the synthesis condition and post-treatment technique the oxygen defects in the Nb-doped NiO_x layer can be also tuned to influence the band structure and bulk resistance for improving the charge separation and transfer of black Si-based photoanode. We design herein a series of experiments to search the origin and enhancement of charge separation and transfer in Nb-doped NiO_x/black Si photoanodes. In these photoanodes, black Si is the primary light absorber and NiO_x-based layer acts as protection layer and hole conducting layer. Cooperative action of Nb doping and plasma treatment markedly increases the charge-separation efficiency (η_{sep}) of the photoanode, while single Nb doping or plasma treatment is lack of this positive effect even deactivating the PEC performance. The concentration and species of oxygen defects in NiO_x-based layer play a crucial role for tuning interfacial electronic band structure and generating hole conductive pathway.

The pristine sample was NiO_x/black Si (NS), while high- (*h*-Nb:NS) and low-concentration Nb-doped NiO_x/black Si (*l*-Nb:NS) were obtained by doping Nb. After 200 or

300 W plasma treatment, the samples were labeled as NS_P₂, *l*-Nb:NS_P₂ and *h*-Nb:NS_P₂ or NS_P₃, *l*-Nb:NS_P₃ and *h*-Nb:NS_P₃, respectively (Supporting Information). Crystal structures of the samples were characterized by the X-ray diffraction (Figure S1, Supporting Information). In NS, three diffraction peaks centered at around 36.9°, 43.0°, and 62.6° were detected, referring to a little shift toward low angle compared with the rhombohedral NiO, indicating the formation of NiO_x layer due to the lattice distortion. After plasma treatment, the peak position of the NiO_x layer is nearly invariable, while the peaks of Nb-doped NiO_x layer shifted toward higher angle. Field emission scanning electron microscopy images and energy dispersive spectroscopy line scan data (Figures S2–S6, Supporting Information) of the samples reveal that the top of black Si (thickness of ≈500 nm) was well filled with NiO_x-based layer for effective separation of black Si and solution. Consequently, Figure 1a schematically illustrates a cross-sectional view of the electrode architecture and the overall oxidation reaction process. Upon light illumination, black Si absorbed photons and produced electrons and holes. Holes were driven through the NiO_x-based layer, oxidizing the hydroxyl group/SO₃²⁻ to oxygen/SO₄²⁻ at the NiO_x-based surface. Electrons were transported to the counter electrode to reduce protons to hydrogen.

The PEC performance of the NiO_x-based/Ni/black Si photoanodes was evaluated by measuring the photocurrent density–potential (*J*–*V*) curves (Figure 1b and Figure S7, Supporting Information) under simulated solar irradiation (AM 1.5G) in 1.0 M aqueous NaOH. In the dark, all photoelectrodes displayed

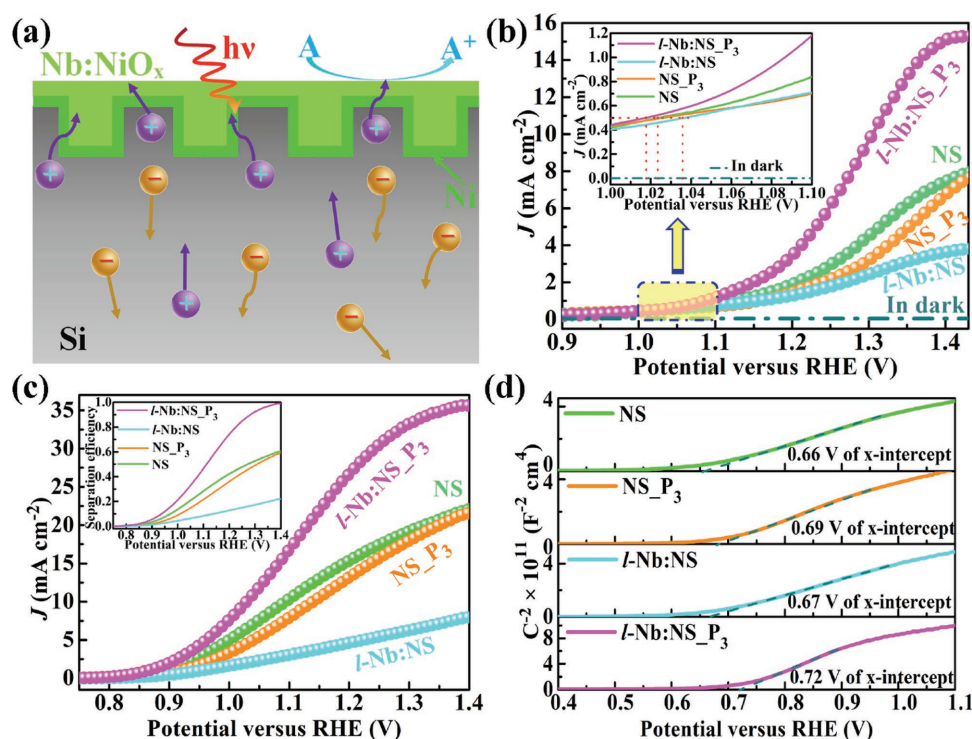


Figure 1. PEC oxidation performance of black Si-based photoanodes. a) Schematic illustration of the charge generation and oxidation reaction in Nb-doped NiO_x/Ni/black Si. b) *J*–*V* curves of the photoanodes under 1 sun illumination in 1.0 M NaOH. c) *J*–*V* curves of the photoanodes for sulfite oxidation measured in phosphate buffer (pH = 7.0) with 1.0 M Na₂SO₃ as the hole scavenger under 1 sun illumination. The inset is the charge-separation efficiencies of photoanodes calculated from sulfite oxidation curves. d) Mott–Schottky plots collected with a frequency of 10 kHz and scan rate of 5 mV s⁻¹.

negligible current versus the potential range. Under illumination, NS just had a J of ≈ 7.9 mA cm⁻² at 1.43 V versus RHE. After plasma treatment, a similar PEC behavior in NS_P₂ and NS_P₃ was observed. However, *l*-Nb:NS with low Nb concentration showed a low J (≈ 3.8 mA cm⁻²) at 1.43 V versus RHE. Surprisingly, the J (15.3 mA cm⁻²) of *l*-Nb:NS_P₃ at 1.43 V versus RHE was about fourfold and twice than that of *l*-Nb:NS and NS, separately. Furthermore, a similar synergistic effect of Nb doping and plasma treatment was also observed in *h*-Nb:NS_P₂ and *h*-Nb:NS_P₃ (Figure S7, Supporting Information). Meanwhile, dry I - V tests of the samples (Figure S8, Supporting Information) made clear their photovoltaic effects and open circuit voltage (V_{oc}), which nearly comply with the PEC oxygen evolution data of the samples. Incident photon-to-current conversion efficiency curves (Figure S9, Supporting Information) and photocurrent density-time (J - t) curves (Figure S10, Supporting Information) of the samples further confirm the joint influence of Nb doping and plasma treatment on PEC performance.

Photocurrent density is synergistically controlled by the light absorption, charge-separation, and charge-injection properties of the photoelectrode.^[5,15,16] Specifically, $J = J_{abs} \times \eta_{sep} \times \eta_{inj}$, where J_{abs} is the J at 100% internal quantum efficiency, η_{sep} is the yield of the photogenerated surface-reaching holes, and η_{inj} is the efficiency of surface-reaching holes that reacted with the electrolyte. To quantify the η_{sep} , J - V curves of sulfite oxidation were measured in phosphate buffer solution (pH = 7.0) with 1.0 M Na₂SO₃ under AM 1.5G illumination (Figure 1c and Figure S11, Supporting Information). PEC sulfite oxidation was a useful tool for assessing charge-separation properties of PEC materials due to the thermodynamically and kinetically more facile reaction process ($\eta_{inj} = 100\%$).^[17] The η_{sep} can be calculated through comparing a series of J following the relationship $\eta_{sep} = J_{sul}/J_{abs}$, where J_{sul} is the J for sulfite oxidation.^[16] The light diffuse reflectance + scattering spectra (Figure S12, Supporting Information) showed little difference with low reflectance (<20%) in the 350–1150 nm region. Besides, the black Si exhibited a bandgap of ≈ 1.1 eV. By integrating the absorbance across AM 1.5G solar spectrum,^[18] J_{abs} of NS, NS_P₃, *l*-Nb:NS, and *l*-Nb:NS_P₃ were calculated to be ≈ 36.6 , 36.8, 36.2, and 36.1 mA cm⁻² (Figure S13, Supporting Information), respectively, suggesting that the discrepancy among the samples is hardly related to light absorption. For *l*-Nb:NS_P₃, J - V curves of sulfite oxidation (Figure 1c) followed the trend of water oxidation with limiting J of 35.6 mA cm⁻² at 1.40 V versus RHE. As shown in the inset of Figure 1c, the substantially higher η_{sep} ($\approx 81\%$) was achieved from *l*-Nb:NS_P₃ at 1.23 V versus RHE than from the other samples. The η_{sep} of $\approx 99\%$ in *l*-Nb:NS_P₃ was acquired at 1.40 V and above versus RHE, which was 350% and 62% higher than that of *l*-Nb:NS ($\approx 22\%$) and NS ($\approx 61\%$), respectively. The η_{sep} values comply well with the variation of J values for the samples in Figure 1b, implying that η_{sep} would be the predominant factor responsible for the enhancement of PEC performance in NiO_x-based/Ni/black Si photoanodes. The Mott-Schottky plots for the samples in Figure 1d were used to determine the flat band voltage. The x -intercepts of the Mott-Schottky plots for NS, NS_P₃, *l*-Nb:NS, and *l*-Nb:NS_P₃ give a flat band voltage of 0.68, 0.71, 0.69, and 0.74 V, respectively. Additionally, N_D of black Si in the samples can be calculated to be 3 – 10×10^{18} cm⁻³ (Supporting Information). Based on Equations (S4)–(S6) in the Supporting

Information, the barrier height of *l*-Nb:NS_P₃ is ≈ 0.80 eV, which is the highest. Generally, a high barrier height can make a contribution to increasing the photovoltage of the photoanode relative to a simple solid-state Schottky barrier.

The elemental feature was studied by X-ray photoelectron spectroscopy (XPS) (Figure S14, Supporting Information). The signal of Si was hardly found on the surface of *l*-Nb:NS_P₃, which means that the black Si was covered completely. The atom ratio of Nb and Ni in *l*-Nb:NS_P₃ and *h*-Nb:NS_P₂ was ≈ 0.014 and 0.103, respectively. In the Ni 2p spectrum (Figure 2a), the peaks at 854.3 and 855.8 eV were assigned to Ni²⁺ and Ni³⁺ in NS. For *l*-Nb:NS, the positions of two peaks shifted toward slightly lower binding energy. After plasma treatment, the peak positions of Ni²⁺ and Ni³⁺ in *l*-Nb:NS_P₃ were reported at 854.4 and 856.0 eV, respectively. In general, the variation of the peak positions is induced by adjusting the chemical environment of this species. Additionally, Raman modes in the Ni–O–Nb vibrations range (790–850 cm⁻¹)^[19] was enhanced for *l*-Nb:NS_P₃ and *h*-Nb:NS_P₂ (Figure S15, Supporting Information). Furthermore, the Nb 3d_{5/2} binding energies of 206.5 and 206.3 eV (Figure 2b) are attributed to Nb⁴⁺ for *l*-Nb:NS and *l*-Nb:NS_P₃, respectively.^[20] Meanwhile, it is clearly observed in Figure S16 in the Supporting Information that all the samples showed a number of defect sites with lower oxygen coordination (Peak β). Among these samples, *l*-Nb:NS_P₃ owned the least defect sites with lower oxygen coordination. On basis of these data, we hypothesize that Nb doping gives rise to slight deficiencies or migration of oxygen surrounded in Ni atoms, while Nb and O of the niobium oxide occupy in the Ni sites and oxygen vacancies of NiO_x lattice after plasma treatment, respectively. The valence band (VB) of NiO_x-based layers was shown in Figure 2c. NS displayed typical VB characteristics of NiO_x, with the edge of the maximum energy at about 0.81 eV. For *l*-Nb:NS and *l*-Nb:NS_P₃, the VB maximum energy blue- and red-shifts toward the vacuum level at approximately 0.76 and 0.97 eV, separately. Optical transmittance of the NiO_x-based layers on cleaned BK7 glass substrates was measured (Figure S18, Supporting Information). Except of *l*-Nb:NS, the transmittance of the samples in the visible–near-infrared wavelength was up to 80%. The direct bandgap, owing to the unoccupied Ni 3d and mixed O 2p/Ni 3d, from extrapolating the linear portion of the Tauc relation ($ah\nu^2$ vs $h\nu$) presented a blueshift before and after plasma treatment, as depicted in Figure 2d. Based on the data of VB maximum and bandgap (3.17 eV), the conduction band (CB) minimum for *l*-Nb:NS_P₃ would occur at about -2.20 eV.

To explore the charge carrier transport, the electrical measurements of the samples were performed by conductive atomic force microscopy (c-AFM) in a vertical configuration. Figure 3a shows AFM topography image (left) and typical I - V curves of marked position by the number (right) for *l*-Nb:NS_P₃. It is apparent that *l*-Nb:NS_P₃ in all the positions possessed the current responses. Among these positions, the positions 1, 3, 4, 5, and 6 have high current (>2 nA), and the current of the other positions was less than 1 nA. Compared with *l*-Nb:NS_P₃, *l*-Nb:NS only had a strong current response (≈ 3 nA) in a certain position (Figure S21, Supporting Information). In addition, there were weak current responses in the range of applied bias for NS and NS_P₃ (Figures S19 and S20, Supporting Information). It should be noted that the free-carrier-like transport

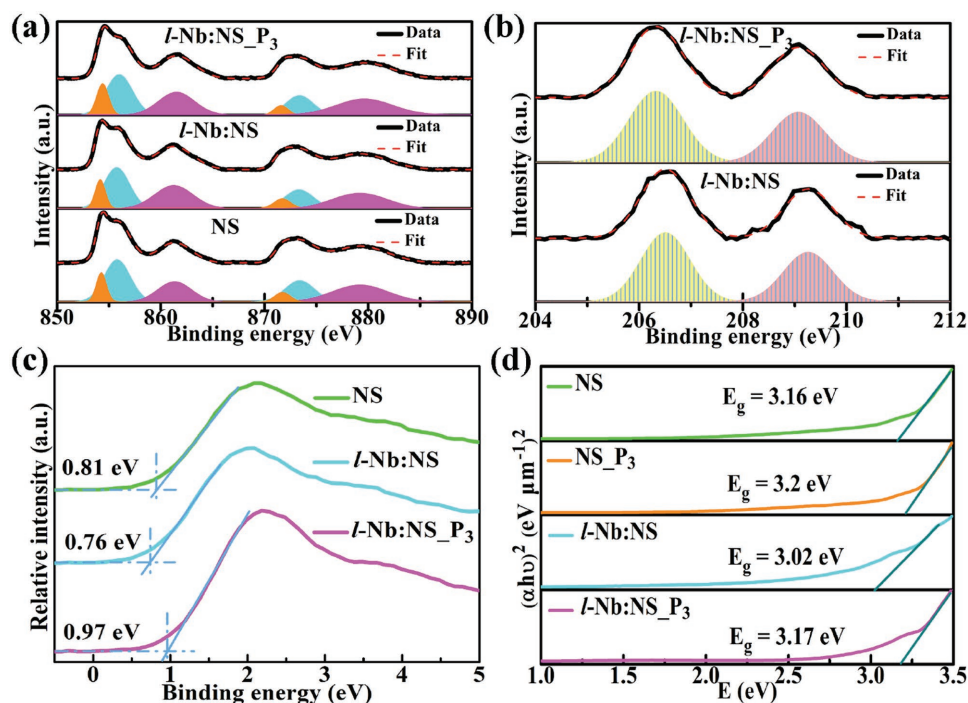


Figure 2. The analysis of the composition and band structure of the samples. a) Ni 2p XPS spectra of NS, *l*-Nb:NS, and *l*-Nb:NS_P₃. b) Nb 3d XPS spectra of *l*-Nb:NS and *l*-Nb:NS_P₃. c) Valence-band XPS spectra of NS, *l*-Nb:NS, and *l*-Nb:NS_P₃. d) Optical absorption coefficients α as a function of the incident photon energy E for direct allowed transition for the NiO_x-based layers of NS, NS_P₃, *l*-Nb:NS, and *l*-Nb:NS_P₃.

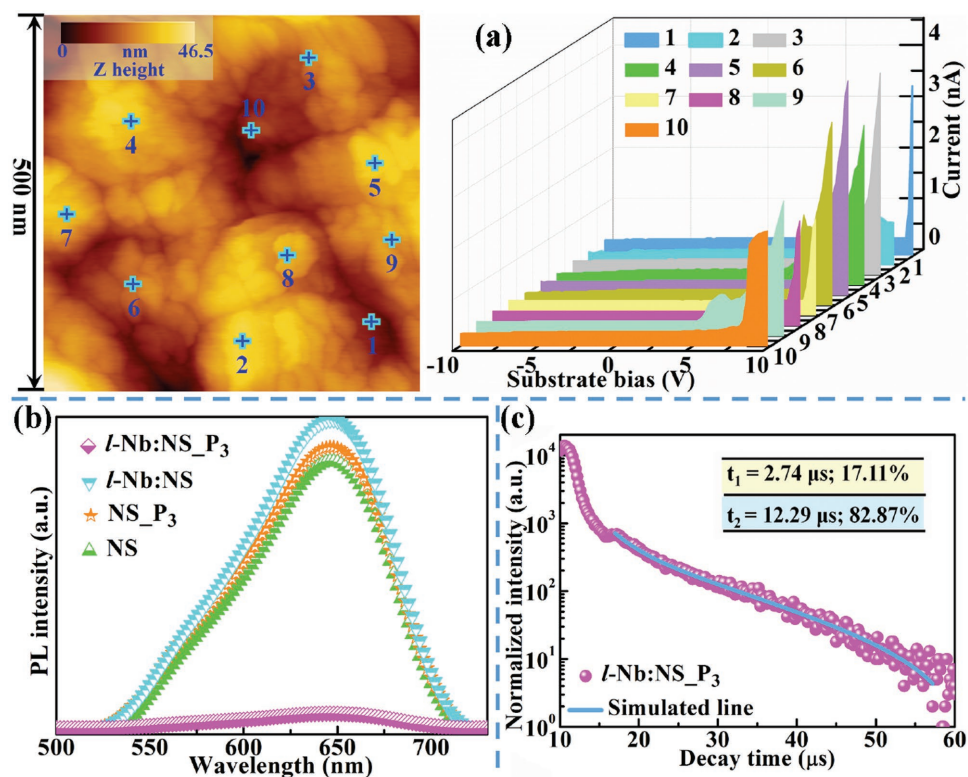


Figure 3. Charge carrier dynamics and paths of the samples. a) AFM topography image (left) and typical I - V curves of marked position by the number (right) for *l*-Nb:NS_P₃. Positions 1–10 in AFM image corresponding to the colored I - V curve. (b) Room-temperature PL spectra of NS, NS_P₃, *l*-Nb:NS, and *l*-Nb:NS_P₃ with excitation wavelength of 405 nm. (c) Time-resolved PL decay curve for *l*-Nb:NS_P₃ at room temperature. The inserted table provides the kinetics parameters.

along domain boundary is absent in the integrated topography AFM and c-AFM imagings (Figure S26, Supporting Information). As a result, the passage of the electric current and the quantity of conductive channels are concurrently increased under a corporate effort of Nb doping and plasma treatment. The photoluminescence (PL) emission spectra are useful to understand the recombination of photogenerated electrons and holes in our samples.^[21] PL peaks of the samples (Figure 3b) were centered at ≈ 650 nm (almost being equivalent to 1.89 eV), which originates from the main emission of bandgap transition as well as recombination of free carriers. A pronounced fluorescence quenching was discovered in *l*-Nb:NS_P₃, meaning the suppression of charge carrier recombination. Time-resolved PL spectra were employed to investigate the charge carrier dynamics of the samples, with the decay curves and kinetics parameters (Figure 3c). The measured charge carrier lifetime shows how long it takes for the electron–hole pairs to decay to their “1/*e*” by radiative recombination. Therefore, longer lifetime usually means slower charge recombination.^[22] Compared with NS (Figure S27, Supporting Information), the PL lifetimes (*t*₂) of *l*-Nb:NS_P₃ was 12.29 μ s, which indicates greatly retarded charge recombination.

Electron paramagnetic resonance (EPR) spectroscopy is a sensitive and nondamaged technique for detecting selectively the defects and states of the materials with unpaired

electrons. As recorded in Figure 4a, a sharp EPR signal, due to the presence of oxygen species with free electrons (namely, oxygen defects), is visible in all samples. However, no resonance signal was assigned to Ni ion species corresponding to *g* values ranging from 2.10 to 2.38.^[23] NS and NS_P₃ showed almost identical EPR signals, which are asymmetric resonance lines at $g_{\perp} \approx 1.9995$. In comparison to NS and NS_P₃, *l*-Nb:NS had a stronger EPR signal, but the values of g_{\perp} were invariable. After plasma treatment, the weakest EPR signal was observed in *l*-Nb:NS_P₃, meanwhile, the g_{\perp} shifted toward the higher *g* value (≈ 1.9997). In addition, similar changes also occurred in EPR signal of *h*-Nb:NS_P₂ (Figure S28, Supporting Information). In EPR spectra, the intensity and *g* value of EPR signals are closely related to the concentration and species of the defects. It is reported that the oxygen vacancy and metal–O[•] of EPR signals are assigned at $g_{\perp} = \approx 1.999$ and 2.000 by simulated EPR data.^[24] As such, the oxygen vacancy and Ni–O[•] can make a joint contribution to EPR signals. When Nb is doped in NiO_x layer, the plasma treatment would trigger the decrease of oxygen vacancies but hardly affect the amount of Ni–O[•]. Therefore, we can envision that the redispersion and reaction of the niobium oxide are induced to fill the oxygen vacancies under plasma treatment. To gain insight into the photoinduced hole-transfer process, in situ EPR experiments were performed before and after illumination at 0 °C (Figures S29–S31,

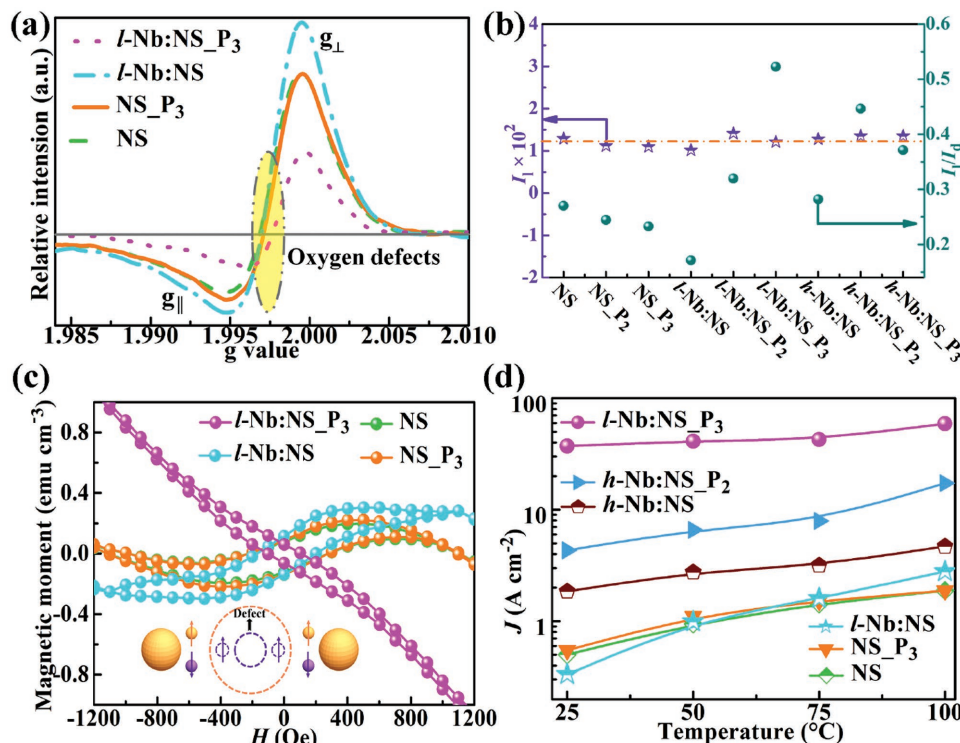


Figure 4. Solid-state characterization of the NiO_x-based/Ni/black Si photoanodes. a) EPR spectra of NS, NS_P₃, *l*-Nb:NS, and *l*-Nb:NS_P₃ at -50 °C. b) The EPR intensity of g_{\perp} under light irradiation (I_l) and the ratio of I_l and I_d (the EPR intensity of g_{\perp} in dark) as a function of the samples. Detailed EPR data are provided in Figures S26–S28 in the Supporting Information. These data are obtained by in situ EPR spectra with and without light irradiation at 0 °C. c) Room-temperature hysteresis curves of NS, NS_P₃, *l*-Nb:NS, and *l*-Nb:NS_P₃ with applied magnetic field perpendicular to the sample surface. These data include the diamagnetic contribution of the Si substrate. The inset is schematic diagram for production of room-temperature ferromagnetism. d) Temperature-dependent current density measurement through the NiO_x-based protection on the black Si substrates. Current measured in a probe station (no electrolyte present) at a Si substrate voltage versus the Ag contact of 2.0 V. Current–voltage data are provided in Figure S31 in the Supporting Information.

Supporting Information). Because of the sensibility of g_{\perp} signal, the changes of g_{\perp} signal are employed to be on behalf of the changes of total EPR signals. Figure 4b shows the EPR intensity of g_{\perp} signal under light irradiation (I_1) and the ratio of I_1 and I_d (the EPR intensity of g_{\perp} signal in dark) as a function of the samples. It is easily found that all the samples possessed an approximate I_1 value of ≈ 125 . The I_1 values remained almost unchanged upon prolonging the irradiation time. **Consequently, for the system of NiO_x -based layer, there are just specified oxygen defects that can play an important role to expedite the migration of light-induced holes.** Furthermore, different samples presented the different ratios of I_1 and I_d , which are proportion to the PEC properties as well as η_{sep} . Among the samples, $l\text{-Nb:NS}_P3$ had the highest ratio of I_1 and I_d (≈ 0.52), **meaning the lowest consumption of photogenerated holes.** As reported previously,^[25] the Ni-O^- anion usually traps a hole to yield a free oxygen radical and then travels quickly from the bulk to the surface which it is transferred to the OH^- to evolve oxygen. But, the free oxygen radical can be captured by the oxygen vacancy to form the stabilized lattice oxygen with no EPR signal.

In diluted magnetic semiconductors, the coupling between the magnetic and the charge transport properties has been studied. The room-temperature ferromagnetism of the samples (Figure 4c) is proportional to the concentration of oxygen defects because the localized nature of the defect sp states fosters the formation of local moments and the extended tails of the defect wave functions induce the long-range coupling between the moments caused by the oxygen defects (inset of Figure 4c).^[26] Interestingly, when the applied magnetic field was parallel with the sample surface, the ferromagnetism of $l\text{-Nb:NS}_P3$ was enhanced distinctly (Figure S33, Supporting Information). The magnetic anisotropy of $l\text{-Nb:NS}_P3$ can facilitate the vertical migration of charge from the inner to the surface during flowing the current.^[27] The intrinsic charge transport properties of the photoanodes were probed by temperature-dependent, metal contact J - V measurements (Figure 4d). The current density for $l\text{-Nb:NS}_P3$ was discovered to have very little dependence on the temperature range from 25 to 75 °C, a strong indication of hole transport by tunneling.^[28] The other samples result in an increasingly temperature-dependent current density in the temperature range, implying a more thermally activated and bulk-limited conduction mechanism.^[28] The significant dependence on the oxygen defects of the measured charge conduction across the NiO_x -based layer illustrates the importance of the synergistic effect of Nb doping and plasma treatment, which adjusts the concentration and species of oxygen defects.

The systematic investigation of the synergistic effect of the Nb doping and plasma treatment in the physicochemical and PEC properties of NiO_x -based layer led to the establishment of the important role of Ni-O^- species for hole transport (Figure 5a). Pure NiO_x is a nonstoichiometric oxide with oxygen defects (like Ni-O^- and oxygen vacancy). Photoinduced hole-transfer process in the NiO_x layer is considered to have two pathways (Figure 5a(i)): transporting the hole to the surface of the photoanodes for oxidation reaction and trapping the active species for the consumption of the holes. Under illumination, the incident photons are absorbed by black Si layer to generate the photoexcited electron-hole pairs, and then the holes are transferred from the black Si layer into the NiO_x layer. The existence of a weak EPR signal

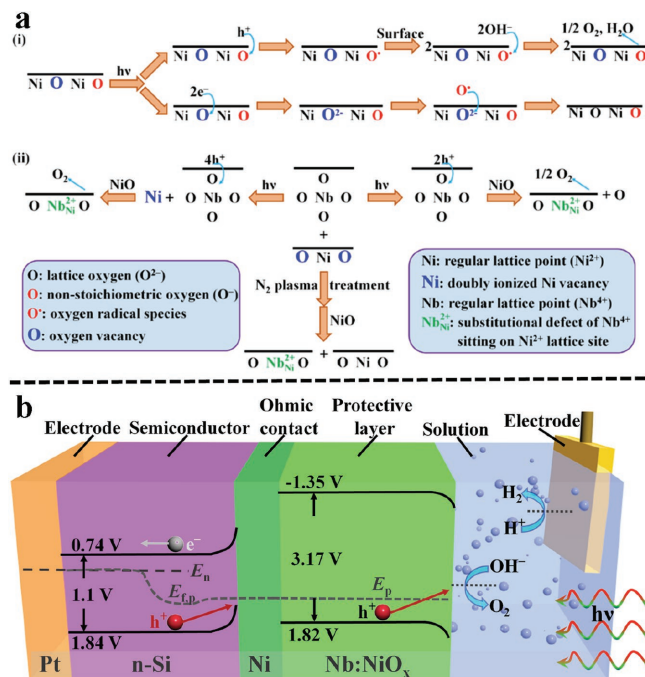


Figure 5. Schematic diagram for NiO_x -based/Ni/black Si photoanode operation based on hole transport and charge separation. a) Proposed reaction mechanism for hole transport over NiO_x -based layer. b) Band structure of the photoanode by plasma treatment. Fermi levels are labeled for the bulk semiconductor and the hole quasi-Fermi level (E_n), the electron quasi-Fermi level (E_{fp}), and the protection layer Fermi level (E_p).

during illumination showed that the active oxygen radicals are responsible for the hole transport, which are active paramagnetic intermediates in metal oxides. The photoinduced hole is most likely linked to a nonstoichiometric O^- anion (Ni-O^-) involving the formation of active oxygen radicals. When the radicals reach at the solid-liquid interface, oxidation reaction takes place on the photoanode surface resulting in the production of O_2 gas. However, the oxygen vacancy is very easy to grasp two photogenerated electrons to yield the negatively charged oxygen vacancy. These vacancies can mainly host the trap centers of active oxygen radicals leading to the consumption of the holes as well as the electron-hole recombination. Nb doping in the NiO_x -based layer primarily produced NbO_2 out of the lattice of NiO_x . First, the introduction of Nb cations into NiO_x creates substitution defects associated with the source of positive holes whose nature decreases the concentration of charge carriers during irradiation, liked Kröger-Vink notation. Furthermore, conductive properties and defect characterization followed by conductive AFM, XPS, in situ EPR was successfully employed for the investigation of the nature of oxygen defects present on the pure and Nb-doped NiO_x layer after plasma treatment. The results exhibited that the oxygen vacancies reduce in the Nb-doped NiO_x layer after plasma treatment. In Figure 5a(ii), it is proposed that the NbO_2 via plasma treatment can replace the Ni lattice sites and fill with oxygen vacancies. Thus, enhanced the hole transport can be realized by synergistic effect of Nb doping and plasma treatment. On the other side, the improvement amplitude in the band structure of NiO_x -based layer can bring about the band energy of the whole photoanode aligned in the favorable direction. The energy band

diagram scheme of the low-concentration Nb-doped NiO_x-based/Ni/black Si photoanode after 300 W plasma treatment is schematized in Figure 5b. The band-edge value in electron volts are converted to electrochemical energy potentials in volts according to the ref. [29]. Here, we illustrate that two tails of the CB minimum and VB maximum are formed to optimize the bandgap of NiO_x-based layer. The tailing effects lead in a suitable band alignment in the photoanode ($E_{g, \text{Si}} = \approx 1.10$ V and $E_{g, \text{NiO}_x} = 3.17$ V), which has the corresponding values of CB minimum (≈ 0.74 V for black Si and -1.35 V for Nb-doped NiO_x) and VB maximum (≈ 1.84 V for black Si and 1.82 V for Nb-doped NiO_x), respectively. In such a situation, black Si and NiO_x-based layer have nearly uniform VB edge. One can infer that a large barrier in CB is capable to block the transport of photoinduced electrons from black Si to NiO_x-based layer, whereas the holes are allowed to go through the VB swimmingly.

In summary, we have proposed a facile two-step route for enhancing the separation and transport of photogenerated charge carriers in the NiO_x-based/Ni/black Si photoanodes by tuning the concentration and species of oxygen defects. The O⁻ plays an important role for facilitating the hole transport. Meanwhile, the optimal band alignment in the NiO_x-based/Ni/black Si photoanode can effectively drive the separation of hole and electron. This work demonstrates that appropriate combined method of metal doping and plasma treatment conducting in the protection layer/Si-based PEC system could be a superior solution to improve the PEC performance instead of traditional and single route. This strategy will find broad application potentials for further advancing the performance in protection layer/semiconductor systems such as photovoltaic devices, sensors, light-emitting diodes, and electrochemical electrodes.

Supporting Information

Supporting Information is available from the Wiley Online Library or from the author.

Acknowledgements

The authors are grateful to the National Natural Science Foundation of China (51402100 and 21573066), the Provincial Natural Science Foundation of Hunan (2016JJ1006 and 2016TP1009), and the Shanghai Sailing Program (17YF1429800).

Conflict of Interest

The authors declare no conflict of interest.

Keywords

charge separation and transfer, doping, oxygen defects, plasma, protection layers

Received: March 20, 2018

Revised: April 18, 2018

Published online: June 19, 2018

- [1] Y. Yan, R. W. Crisp, J. Gu, B. D. Chernomordik, G. F. Pach, A. R. Marshall, J. A. Turner, M. C. Beard, *Nat. Energy* **2017**, *2*, 17052.
- [2] M. J. Kenney, M. Gong, Y. Li, J. Z. Wu, J. Feng, M. Lanza, H. Dai, *Science* **2013**, *342*, 836.
- [3] J. Cen, Q. Wu, M. Liu, A. Orlov, *Green Energy Environ.* **2017**, *2*, 100.
- [4] J. Oh, H. C. Yuan, H. M. Branz, *Nat. Nanotechnol.* **2012**, *7*, 743.
- [5] Y. Yu, Z. Zhang, X. Yin, A. Kvit, Q. Liao, Z. Kang, X. Yan, Y. Zhang, X. Wang, *Nat. Energy* **2017**, *2*, 17045.
- [6] R. Liu, Z. Zheng, J. Spurgeon, X. Yang, *Energy Environ. Sci.* **2014**, *7*, 2504.
- [7] D. Bae, B. Seger, P. C. Vesborg, O. Hansen, I. Chorkendorff, *Chem. Soc. Rev.* **2017**, *46*, 1933.
- [8] K. Sun, N. Park, Z. Sun, J. Zhou, J. Wang, X. Pang, S. Shen, S. Y. Noh, Y. Jing, S. Jin, P. K. L. Yu, D. Wang, *Energy Environ. Sci.* **2012**, *5*, 7872.
- [9] K. Sun, F. H. Saadi, M. F. Lichterman, W. G. Hale, H. P. Wang, X. H. Zhou, N. T. Plymale, S. T. Omelchenko, J. H. He, K. M. Papadantonakis, B. S. Brunshwig, N. S. Lewis, *Proc. Natl. Acad. Sci. U. S. A.* **2015**, *112*, 3612.
- [10] F. A. L. Laskowski, M. R. Nellist, R. Venkatkarthick, S. W. Boettcher, *Energy Environ. Sci.* **2017**, *10*, 570.
- [11] L. Trotochaud, S. L. Young, J. K. Ranney, S. W. Boettcher, *J. Am. Chem. Soc.* **2014**, *136*, 6744.
- [12] K. Sun, Y. J. Kuang, E. Verlage, B. S. Brunshwig, C. W. Tu, N. S. Lewis, *Adv. Energy Mater.* **2015**, *5*, 1402276.
- [13] K. Sun, X. L. Pang, S. H. Shen, X. Q. Qian, J. S. Cheung, D. L. Wang, *Nano Lett.* **2013**, *13*, 2064.
- [14] L. Ji, H. Y. Hsu, X. Li, K. Huang, Y. Zhang, J. C. Lee, A. J. Bard, E. T. Yu, *Nat. Mater.* **2017**, *16*, 127.
- [15] F. Wu, Y. Yu, H. Yang, L. N. German, Z. Li, J. Chen, W. Yang, L. Huang, W. Shi, L. Wang, X. Wang, *Adv. Mater.* **2017**, *29*, 1701432.
- [16] T. W. Kim, K. S. Choi, *Science* **2014**, *343*, 990.
- [17] Y. S. Chen, J. S. Manser, P. V. Kamat, *J. Am. Chem. Soc.* **2015**, *137*, 974.
- [18] W. Yang, Y. Yu, M. B. Starr, X. Yin, Z. Li, A. Kvit, S. Wang, P. Zhao, X. Wang, *Nano Lett.* **2015**, *15*, 7574.
- [19] I. Nowak, M. Ziolk, *Chem. Rev.* **1999**, *99*, 3603.
- [20] S. Zhang, S. B. Ogale, W. Yu, X. Gao, T. Liu, S. Ghosh, G. P. Das, A. T. S. Wee, R. L. Greene, T. Venkatesan, *Adv. Mater.* **2009**, *21*, 2282.
- [21] J. Zheng, S. Bao, X. Zhang, H. Wu, R. Chen, P. Jin, *Appl. Catal., B* **2016**, *183*, 69.
- [22] J. Chen, C. L. Dong, D. Zhao, Y. C. Huang, X. Wang, L. Samad, L. Dang, M. Shearer, S. Shen, L. Guo, *Adv. Mater.* **2017**, *29*, 1606198.
- [23] A. Rosencwaig, G. K. Wertheim, H. J. Guggenheim, *Phys. Rev. Lett.* **1971**, *27*, 479.
- [24] F. Liu, N. Feng, Q. Wang, J. Xu, G. Qi, C. Wang, F. Deng, *J. Am. Chem. Soc.* **2017**, *139*, 10020.
- [25] Z. Skoufa, E. Heracleous, A. A. Lemonidou, *J. Catal.* **2015**, *322*, 118.
- [26] Y. Liu, G. Wang, S. Wang, J. Yang, L. Chen, X. Qin, B. Song, B. Wang, X. Chen, *Phys. Rev. Lett.* **2011**, *106*, 087205.
- [27] K. Cai, M. Yang, H. Ju, S. Wang, Y. Ji, B. Li, K. W. Edmonds, Y. Sheng, B. Zhang, N. Zhang, S. Liu, H. Zheng, K. Wang, *Nat. Mater.* **2017**, *16*, 712.
- [28] Y. W. Chen, J. D. Prange, S. Duhnen, Y. Park, M. Gunji, C. E. Chidsey, P. C. McIntyre, *Nat. Mater.* **2011**, *10*, 539.
- [29] Z. Wang, C. Yang, T. Lin, H. Yin, P. Chen, D. Wan, F. Xu, F. Huang, J. Lin, X. Xie, M. Jiang, *Adv. Funct. Mater.* **2013**, *23*, 5444.